High-Energy-Density Plasma Nanorod by Collisionless Absorption of Ultrafast Laser Pulse Inside Dielectrics

Kazem Ardaneh,[1,2] Remi Meyer,[1] Mostafa Hassan,[1] Remo Giust,[1] Chen Xie,[3] Benoit Morel,[1] Ismail Ouadghiri-Idrissi,[1] Luca Furfaro,[1] Luc Froehly,[1] Arnaud Couairon,[4] Guy Bonnaud,[5] and Francois Courvoisier[1]

[1]*Université Marie et Louis Pasteur, CNRS, institut FEMTO-ST, F-25000 Besançon, France*
[2]*Sorbonne University, CNRS, IPSL Climate Modeling Center, Pierre and Marie Curie Campus, 4 place Jussieu, 75252 Paris, France*
[3]*Key Laboratory of Opto-electronic Information Technology of Ministry of Education, School of Precision Instruments and Opto-electronics Engineering, Tianjin University, 300072 Tianjin, China*
[4]*CPHT, CNRS, Ecole Polytechnique, Institut Polytechnique de Paris, Route de Saclay, F-91120 Palaiseau, France*
[5]*CEA, Centre de Paris-Saclay, DRF, Université Paris-Saclay, 91191 Gif-sur-Yvette, France*

(Received 6 November 2024; accepted 8 July 2026; published 10 September 2026)

The generation of energetic and dense plasmas by femtosecond laser pulses within the bulk of solids can pave the way to study warm dense matter, shocks, extreme UV radiation, or the synthesis of new material phases. However, this has remained elusive because of the intrinsic dynamical effects of defocusing by the laser-generated plasma. Here, we demonstrate the generation of overcritical plasma densities inside transparent solids over long distances. We identify with experiments in bulk sapphire and first-principles simulations that femtosecond conical interference via a Bessel beam creates a dense plasma rod of typically less than 400 nm diameter. We show that collisionless resonance absorption plays a primary role in the energy deposition process, yielding a plasma with an energy density on the order of $\mathrm{MJ/cm^3}$, whose length can reach several cm using only tabletop femtosecond lasers. This opens new avenues for developing high-energy-density physics within solids.

DOI: 10.1103/k23j-c9y7

The creation of dense and energetic plasmas by ultrafast laser pulses is crucial for the studies of warm dense matter [1–4], laser-induced shocks, laser nanofabrication [5], or for the synthesis of new materials via for example localized microexplosions [6,7]. The formation of dense plasma by ultrashort laser pulses has been widely investigated at the *surface* of solids. However, to unlock new opportunities in confined geometry and over long distances, it is desirable to generate such plasmas *inside* solids. For instance, this could enable a significant path length for an ultrafast x-ray pulse to probe matter in the regime of high energy density. However, when focussing a Gaussian beam in the bulk of transparent solids, the electron-hole plasma generated by nonlinear ionization at early stage in the pulse propagation deviates most of the laser pulse energy from the focal region. It impedes reaching high peak intensities at the focus. Hence, conventional Gaussian beams fail to create plasma with high density over lengths exceeding several micrometers.

Zeroth-order Bessel beams offer a new route. They correspond to a circularly symmetric interference field generated by a conical distribution of wave vectors. Their transverse intensity consists of a bright "diffraction-free" [8] central core surrounded by concentric side lobes. The central core length is independent of its diameter. The conical flow of light uniformly distributes energy along the plasma created in the central core early within the ultrafast laser pulse, as shown in Fig. 1(a). In contrast with Gaussian beams, Bessel beams are nearly insensitive to the spherical aberration and to the distortions generated by the nonlinear Kerr effect [9]. Via a single 100 fs pulse, we open an extremely long (up to 1 cm) void nanochannel in glass [10,11], or sapphire [12].

However, because directly measuring the plasma density within the bulk of the material at subwavelength scale remained impossible, the typical plasma density reached in the void formation regime is still under controversy, even 15 years after the first demonstration. The microexplosion mechanism for void formation hypothesizes an overcritical plasma density [13] while a scenario based on cavitation in a liquid phase [14] would instead advocate for relatively low-density plasma. The latter scenario was supported by several numerical simulations showing low absorption, generation of plasma density well below the critical density (density at which the total permittivity drops to zero), and with a relatively large diameter exceeding 1 μm [15–17], but incompatible with the narrow diameter of voids and the high absorption experimentally observed [18]. This suggests another phenomenon occurs during the interaction, not captured by pulse propagation or hydrocode approaches [16,19].

Here, we show that, in fact, the mechanism at stake is the collisionless resonance absorption mechanism which occurs in this femtosecond Bessel beam configuration in

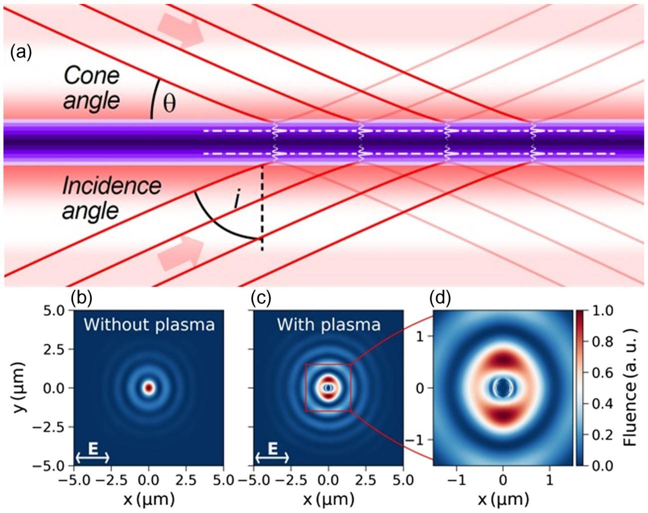

FIG. 1. Interaction of a Bessel beam with a plasma rod. (a) The Bessel beam wave components impinge conically toward the optical axis. Wave turning (reflection) occurs at the plasma density indicated in light purple slightly away from the optical axis. In the plane of polarization, wave conversion can occur and excites resonance absorption around the critical density layer shown as a white dashed line. (b),(d) Near-field fluence distribution in xy plane at $z = 7$ μm (peak of the axial fluence profile) from PIC simulations, (b) in the absence of plasma, and (c) in the presence of a circularly-symmetric plasma rod with a transverse Gaussian density profile. The input polarization is horizontal. (d) Enlarged view of the central part of (c).

the bulk dielectrics and plays a critical role in the energy deposition process. We demonstrate the creation of overcritical plasmas with femtosecond Bessel beams in sapphire, using only a moderately high numerical aperture (0.4). The resonance explains the very high (50%) absorption that we experimentally measured, as will be detailed later. Resonance absorption has been widely studied in the context of inertial confinement fusion by illuminating the surface of solids [20–23]. It takes place when a laser pulse obliquely impinges on a plasma density ramp, and the laser electric field has a component parallel to the plasma density gradient. In such conditions, mode conversion resonantly drives electron plasma waves at the critical surface [white dashed lines in Fig. 1(a)], which are damped via Landau damping. The overall process efficiently transfers the laser pulse energy into the plasma via a collisionless mechanism. Importantly, this physical process cannot be correctly captured by conventional models of laser-matter interaction which neglect longitudinal plasma waves and non-Maxwellian distributions of free electrons.

Here, we compare several complementary experimental diagnostics to first-principles particle-in-cell (PIC) simulations using the 3D massively parallel code EPOCH [24]. First, we determine the typical transverse plasma density profile generated by the Bessel beam in the illumination conditions corresponding to void formation. While conventional models for laser pulse absorption in dielectrics have hitherto relied on collisional processes (inverse Bremsstrahlung), we demonstrate that most of the absorption is here due to a collisionless mechanism. The observation of second harmonic generation from the bulk in the single shot regime additionally confirms the resonance absorption process.

The interaction of an ultrashort pulse with a dielectric medium can be viewed as a two-stage process. In the first stage, field ionization and electron-impact ionization create an electron-hole plasma, with which the trailing part of the laser pulse interacts during the second stage. We will investigate the intensity regime where femtosecond Bessel beam open voids inside sapphire [12]. The length of the laser-generated plasma is linearly controlled by the length of the Bessel beam. In the experiments described below, the plasma has a length of 18 μm with a typical diameter of a few hundred nanometers and it absorbs approximately 50% of the 1 μJ pulse energy. The ionization energy absorbed to produce an overcritical plasma of this size is $n_c V U_g$ where n_c is the critical density at 800 nm, $V \approx 2\ \mu\text{m}^3$ the plasma volume and $U_g \approx 10$ eV the bandgap of sapphire. This ionization energy is less than 0.04 μJ which is negligible compared to the total absorbed energy. Therefore, we hypothesize that the first stage is very short compared to the pulse duration and focus our modeling efforts on the second stage of the interaction. Our model does not take into account ionization in order to isolate the laser-plasma interaction.

We have performed 3D PIC simulations to model the interaction of a 100 fs Bessel beam with a plasma rod with a transversely Gaussian density profile and longitudinally homogeneous profile (see End Matter). The pulse, with a central wavelength $\lambda = 800$ nm, propagates along the z direction and is linearly polarized along the x direction [25]. Since the conical interaction is nearly z-invariant, we limit the length of the Bessel beam simulated numerically to half of the experimental one, to reduce the computing load. In the absence of plasma, the intensity reaches $6 \times 10^{14}\ \text{W/cm}^2$, as in the experiments. The beam cone (half-apex) angle is $\theta = 25°$, which corresponds to an incidence angle $i = 65°$ on the cylindrical surface of the plasma. Figure 1(b) shows the fluence distribution, i.e., the time integration of the Poynting vector of the Bessel beam, in the transverse xy plane at a propagation distance corresponding to the peak of axial fluence profile, without plasma.

In the central lobe, the amplitude of the z component of the electric field is 25% of the x component, while the y component remains negligible (2%).

We first qualitatively describe the physics of Bessel beam interaction with a circularly symmetric overcritical plasma, as shown in Fig. 1(c). The enlarged view [Fig. 1(d)] shows two high-intensity structures that appear inside the region of the initial central lobe. One is composed of two electromagnetic lobes outside the plasma ($y = \pm 0.5$ μm), oriented perpendicular to the pulse polarization. It originates from the difference in permittivity between the plasma rod and the external medium [26,27]. It amplifies the field perpendicularly to the polarization. The second structure is highly localized around the critical surface and shows two lobes along the polarization direction. It corresponds to resonantly driven electrostatic plasma waves at the critical surface. Importantly, this structure cannot be observed experimentally by beam imaging since the electrostatic fields do not propagate outside the sample. In the following figures, we exclude the electrostatic field components from the simulated fluence distributions.

Another phenomenon occurs, shown in Fig 1(a), and will be used as an experimental diagnostic: wave turning. When a plane wave impinges on a plasma density gradient, reflection occurs where the local refractive index reaches total internal reflection condition for incidence angle i. This is at the density $n(r_t) = n_c \cos^2 i$, where n_c is the critical density in the medium and r_t is the turning point radius. This is effectively the phenomenon underlying the general term "defocusing effect." We show in Supplemental Material (SM) [28], using a multilayer electromagnetic solver, that wave turning shifts the side lobes of the Bessel beam by at least r_t. This provides an indirect measurement of the plasma radius at the turning point density $n(r_t) = 0.057 n_c$ that will be used below. In the PIC simulation of Fig. 1(c), the beam interacts with an overcritical circular plasma rod with a turning point radius of 274 nm. We observe that all side lobes are effectively shifted outward by a distance of about 350 nm.

Therefore, near-field imaging provides a good experimental mean to measure the wave-turning radius. Our setup is described in the End Matter (Fig. 4). The 100 fs Bessel pulse is positioned inside the sapphire sample so as to cross the sapphire exit surface at a distance z. A microscope objective collects the pulse after interaction and we image on a CCD the near-field fluence distribution for propagation distance z [Figs. 2(a) and 2(b)].

Importantly, since the Bessel beam conically impinges on the longitudinal plasma rod, the reflected and transmitted pulse are both forward propagating and collected by the high-numerical aperture microscope objective. We experimentally verified that backscattering is actually negligible (see SM [28]). Thomson scattering is negligible with an efficiency below 10^{-6} (see SM [28]). Therefore, the evolution of energy along propagation can be measured by spatially integrating on the camera the fluence at each z. The overall absorption has been confirmed by measuring pulse energy with large-area photodiodes, as in reference [18].

Figures 2(a) and 2(b) show the resulting fluence distribution, respectively, in the linear, low energy regime (a) and for a pulse energy of 1 μJ [(b), void formation regime]. A lobe shift of typically 200 nm appears, as indicated by the orange dashed lines. We obtain the important information that the turning radius r_t, along the polarization direction, is within the range 100–250 nm (see Fig. S5 [28]). Although our measurement is time-integrated, it provides an order of magnitude of the plasma scale during the pulse, since we numerically observed that plasma reshaping is negligible over this timescale. Therefore, the plasma is extremely confined around the optical axis. Figure 5 (top) shows the fluence distribution in the zx plane: the nearly constant lobe shift confirms the plasma confinement all along the beam.

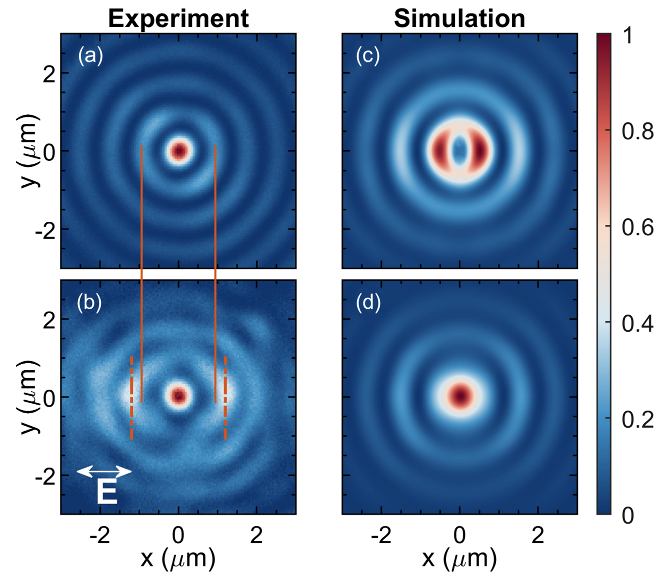

FIG. 2. (a),(b) Experimental fluence in xy plane at $z = 20$ μm recorded (a) in the linear regime and (b) for a 1 μJ pulse. The orange solid (resp. dashed) lines show the position of the first lobe in the linear (resp. nonlinear) regime, highlighting the shift due to the wave-turning effect. (c) Slice of the PIC simulated fluence in the nonlinear regime in the sample, where longitudinal fields have been removed. (d) Same as (c) with postprocessing to simulate the effect of imaging of the fields on the camera, with 1 μm positioning error of the imaging setup. In a Bessel beam, the number of side lobes follows the beam length. Thus the simulation shows fewer lobes than the experiment. The period is the same in (b) and (d): 0.8 ± 0.1 μm.

The plasma diameter is significantly smaller than what was reported numerically from previous literature, and the lobe shift measured experimentally on the fluence distribution is also much smaller than what was numerically predicted for similar focusing conditions [15–17]. We remark that in Fig. 2(b) the central peak is not split as one could expect from the simulation [Fig. 2(c)], but we will explain and model this imaging artifact in a subsequent section [Fig. 2(d)].

The evolution of the pulse energy as a function of propagation distance, shows a significant energy drop of nearly 50% over an 18 μm segment of propagation [see End Matter Fig. 5 (bottom)]. It corresponds to the region where plasma is generated and is approximately the length of the void channel created in sapphire under similar laser

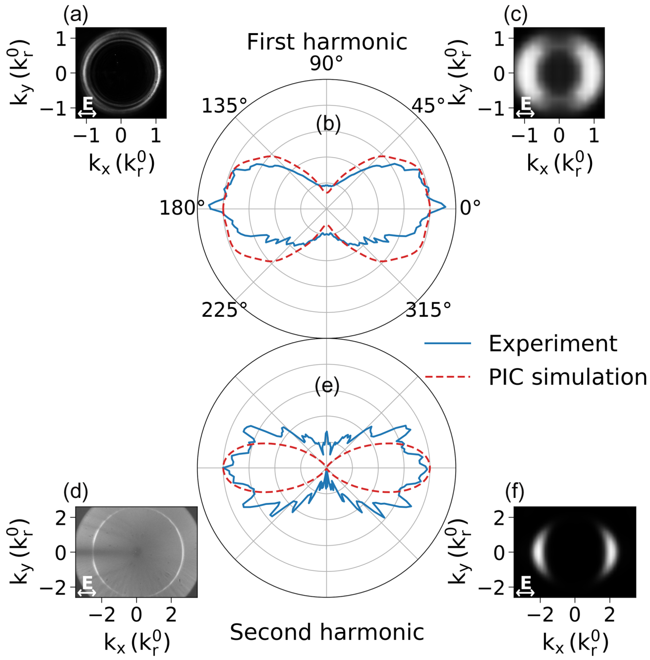

FIG. 3. (a) Experimental far-field distribution of the laser pulse interaction with the sample. (b) Experimental and numerical angular distributions of the far-field distributions. (c) Numerical far-field distribution. (d) Experimental far-field emission distribution in the spectral range 400 ± 20 nm, where the second harmonic appears as two intense lobes and black-body radiation as a uniform background filling the numerical aperture of the imaging. (e) Experimental and numerical angular distributions of the second harmonic. (f) Numerical far-field emission distribution of the second harmonic. In (a), (d) the axes are normalized by the radial component of the Bessel pulse, $k_r^0 = 2\pi \sin\theta/\lambda$, where $\theta = 25°$ is the beam cone angle.

illumination conditions [12]. This confirms the localization of energy deposition in the high-intensity region, i.e., not in an earlier stage of the propagation as often observed with Gaussian beams [36,37].

In the linear, absorption-free regime, the far-field fluence of a Bessel beam is a homogeneous ring. Figure 3(a) shows the experimental far-field fluence distribution collected after the interaction. Its angular distribution is shown in Fig. 3(b) (solid blue line). It shows two lobes oriented in the direction of the input pulse polarization. This constitutes a third diagnostic.

We have then determined the *typical* plasma density profile via a series of numerical simulations with different transversely Gaussian profiles, for which we adjusted peak and width to match all previous experimental diagnostics (Bessel lobe shift, absorption, asymmetries in near- and far-field fluence distributions). The small lobe shift and hence small wave-turning radius r_t impose a small plasma diameter. In this condition, undercritical densities lead to low absorption and axially symmetric far-field distributions. Overall, only an overcritical plasma with an elliptically shaped cross section could fit all diagnostics simultaneously. Figure S6 [28] compares a series of different simulation results. The best quantitative agreement is obtained for a plasma with a peak density of about $5n_{cr}$, critical radius r_c of 190 nm (turning radius $r_t = 274$ nm) along the polarization direction and $r_c = 450$ nm perpendicular to the polarization. The red dashed curve on Fig. 3(b) shows the numerical far-field distribution with the same asymmetry as in the experimental case. Importantly, the far-field distributions of Fig. 3 are thicker numerically than experimentally because the Bessel zone is shorter in the simulation (thicker Fourier- transform). While a non-Gaussian transverse plasma profile could have led to slightly different values of peak density and turning radius, our results provide representative orders of magnitude.

The ellipticity can be explained by the field amplification perpendicular to the polarization during the plasma buildup phase [26,27]. We experimentally confirmed that the plasma is elliptical and elongated perpendicular to the polarization by SEM imaging of voids formed in sapphire after the laser-induced microexplosion, as shown for different input polarization directions in Fig. S1 [28].

Our simulations also agree well with the experiments in terms of absorption: it is 54% using a collisional model. In Fig. S7 [28], we show the evolution of pulse energy with propagation distance: it decreases quasilinearly as in experiments. In Fig. 2(c), our simulation of the near field fluence retrieves the same asymmetries and a ≈400 nm lobe shift of the Bessel beam as in the experiments. Importantly, this shift could be reduced by using hyper-Gaussian plasma density distribution instead of Gaussian.

The central peak in the experimental profile [Fig. 2(b)], however, does not show a narrow internal dip as in the numerical one [Fig. 2(c)]. Obviously, since our numerical simulation does not model the first ionization stage, it does not account for the fraction of the laser pulse energy which travels in the linear regime through the sample before the ionization onset and generates on the camera a high-intensity central lobe. We found out that the discrepancy can be fully attributed to the imaging process. First, the limited numerical aperture of the imaging microscope objective (0.9) filters out the finest features of the local fields inside the plasma. Second, the slight 1 μm error in the distance between the sample and the focal plane of the imaging microscope objective impacts the final fluence distribution. We used the approach of Ref. [29] to post-process our numerical simulations and include these effects in our modeling (see SM [28]), as shown in Fig. 2(d). We now obtain a good agreement with our experimental results.

The generation of overcritical plasma density during the pulse duration has important physical consequences because resonance absorption can take place. We have repeated the PIC simulations in a collisionless configuration and obtain quasi-identical results. The evolution of the pulse energy as a function of propagation distance for both cases is compared in Fig. S7 [28]. The difference is only a few percent (5 points), we conclude that the primary absorption mechanism is *collisionless* resonance absorption [20–22]. The collisionless Landau effect is responsible for damping the electron plasma waves generated at the critical surface [38]. This phenomenon cannot be captured by the models used hitherto to simulate pulse propagation in dielectrics.

A second significant result is that we experimentally observed second harmonic emission from the bulk of sapphire despite its zero second-order nonlinear susceptibility [39]. Although the second harmonic emission could arise from higher-order susceptibilities, it is observed in our laser-plasma simulation, that does not include nonlinear permittivity other than plasma coupling. We experimentally imaged the far-field fluence distribution in the spectral range 400 ± 20 nm (see SM [28]) as shown in Fig. 3(d). The signal is composed of a low-intensity background from black-body radiation and a thin second harmonic emission oriented at an angle nearly identical to the pump and polarized as the pump. Figure 3(e) shows the very good agreement between experimental results and our PIC simulations, using the same parameters as before. In the simulations, the ratio of the second harmonic to the fundamental intensity is approximately $\sim 10^{-5}$.

In conclusion, we have demonstrated (i) that ultrafast Bessel beams can generate overcritical plasma within the bulk of sapphire *during* the 100 fs pulse, (ii) that collisionless resonance absorption is a crucial process for energy deposition, and (iii) the second harmonic emission in single shot regime from the bulk of sapphire. The importance of the collisionless character of the absorption process can be additionally coined by the fact that a plasma hydrodynamic code [40], failed to reproduce our experimental results: although full Maxwell's equations are solved, a conventional hydrocode does not capture essential collisionless processes associated to the non-Maxwellian distribution of the electron density, such as Landau damping.

Our findings answer a central question about energy deposition by ultrafast pulses within the bulk of solids, which is particularly crucial for modeling laser-solid interaction with Bessel or new beam shapes. Nanoplasma generation with overcritical density inside solids opens interesting opportunities for nonlinear plasmonics [41], nonlinear optics with epsilon-near-zero materials [42], generation of strong THz fields [43], and extreme ultraviolet sources [44].

Our results also open a new route to generate high energy density matter inside solids, in a geometry where the material is confined and cannot expand into vacuum. The energy density deposited in our experiments is on the order of $\mathrm{MJ/cm^3}$, which is a typical range for driving a transformation from solid to warm dense matter [45,46]. Since the conical shape of the Bessel beam is propagation invariant, our results can be extended to much longer propagation distances: increasing laser pulse energy to 1 mJ is enough to create, at timescale of 100 ps after the pulse, a 1 cm warm dense matter rod in identical conditions as discussed above [11]. This corresponds to relatively large volume of warm dense matter on the order of 1000 $\mu\mathrm{m}^3$. This approach therefore provides a convenient new platform for exploring warm dense matter physics.

Acknowledgments—K. A., R. M., and M. H. equally contributed, with the largest fraction of, respectively, simulation work, experimental work, and imaging techniques. Technical assistance by C. Billet and E. Dordor as well as fruitful discussions with J. M. Dudley and D. Brunner are gratefully acknowledged. We thank the EPOCH support team for help ([47]) and French RENATECH network. The authors acknowledge the financial supports of the European Research Council (ERC) 682032-PULSAR, Region Bourgogne-Franche-Comte and Agence Nationale de la Recherche (EQUIPEX+ SMARTLIGHT platform ANR-21-ESRE-0040), Labex ACTION ANR-11-LABX-0001-01, I-SITE BFC project (contract ANR-15-IDEX-0003), and the EIPHI Graduate School ANR-17-EURE-0002. This work was partly supported by the french RENATECH network and its FEMTO-ST technological facility. This work was also granted access to the PRACE HPC resources at CINECA, Italy, under the Project "PULSARPIC" (PRA19_4980), PRACE HPC resource at TGCC, France under the Project "PULSARPIC" (RA5614), HPC resource at TGCC, France under the projects A0070511001 and A0090511001, and Mésocentre de Calcul de Franche-Comté.

Data availability—The data that support the findings of this article are available from the authors upon reasonable request.

[1] T. Guillot, Interiors of giant planets inside and outside the solar system, Science **286**, 72 (1999).
[2] E. G. Saiz *et al.*, Probing warm dense lithium by inelastic x-ray scattering, Nat. Phys. **4**, 940 (2008).
[3] K. Falk, Experimental methods for warm dense matter research, High Power Laser Sci. Eng. **6**, e59 (2018).
[4] T. Dornheim, J. Vorberger, and M. Bonitz, Nonlinear electronic density response in warm dense matter, Phys. Rev. Lett. **125**, 085001 (2020).
[5] Z.-Z. Li, L. Wang, H. Fan, Y.-H. Yu, Q.-D. Chen, S. Juodkazis, and H.-B. Sun, O-FIB: Far-field-induced near-field breakdown for direct nanowriting in an atmospheric environment, Light Sci. Appl. **9**, 41 (2020).
[6] A. Vailionis, E. G. Gamaly, V. Mizeikis, W. Yang, A. V. Rode, and S. Juodkazis, Evidence of superdense aluminium synthesized by ultrafast microexplosion, Nat. Commun. **2**, 445 (2011).
[7] L. A. Smillie, M. Niihori, L. Rapp, B. Haberl, J. S. Williams, J. E. Bradby, C. J. Pickard, and A. V. Rode, Exotic silicon phases synthesized through ultrashort laser-induced

microexplosion: Characterization with Raman microspectroscopy, Phys. Rev. Mater. **4**, 093803 (2020).
[8] J. Durnin, J. J. Miceli, and J. H. Eberly, Diffraction-free beams, Phys. Rev. Lett. **58**, 1499 (1987).
[9] P. Polesana, M. Franco, A. Couairon, D. Faccio, and P. Trapani, Filamentation in Kerr media from pulsed Bessel beams, Phys. Rev. A **77**, 043814 (2008).
[10] M. K. Bhuyan, F. Courvoisier, P. A. Lacourt, M. Jacquot, R. Salut, L. Furfaro, and J. M. Dudley, High aspect ratio nanochannel machining using single shot femtosecond Bessel beams, Appl. Phys. Lett. **97**, 081102 (2010).
[11] R. Meyer, L. Froehly, R. Giust, J. D. Hoyo, L. Furfaro, C. Billet, and F. Courvoisier, Extremely high-aspect-ratio ultrafast Bessel beam generation and stealth dicing of multi-millimeter thick glass, Appl. Phys. Lett. **114**, 201105 (2019).
[12] L. Rapp, R. Meyer, R. Giust, L. Furfaro, M. Jacquot, P. A. Lacourt, J. M. Dudley, and F. Courvoisier, High aspect ratio micro-explosions in the bulk of sapphire generated by femtosecond Bessel beams, Sci. Rep. **6**, 34286 (2016).
[13] S. Juodkazis, K. Nishimura, S. Tanaka, H. Misawa, E. G. Gamaly, B. Luther-Davies, L. Hallo, P. Nicolai, and V. T. Tikhonchuk, Laser-induced microexplosion confined in the bulk of a sapphire crystal: Evidence of multimegabar pressures, Phys. Rev. Lett. **96**, 166101 (2006).
[14] M. K. Bhuyan, M. Somayaji, A. Mermillod-Blondin, F. Bourquard, J. P. Colombier, and R. Stoian, Ultrafast laser nanostructuring in bulk silica, a “slow” microexplosion, Optica **4**, 951 (2017).
[15] P. K. Velpula, M. K. Bhuyan, F. Courvoisier, H. Zhang, J. P. Colombier, and R. Stoian, Spatio-temporal dynamics in nondiffractive Bessel ultrafast laser nanoscale volume structuring, Laser Photonics Rev. **10**, 230 (2016).
[16] C. Xie, R. Giust, J. Zhang, V. Jukna, R. Meyer, L. Furfaro, M. Jacquot, L. Froehly, J. M. Dudley, A. Couairon, and F. Courvoisier, Enhanced absorption and plasmon excitation in the bulk of fused silica with femtosecond bessel beams, in *Conference on Lasers and Electro-Optics* (Optica Publishing Group, Washington, DC, 2016), p. STh3Q.2.
[17] K. Mishchik, R. Beuton, O. D. Caulier, S. Skupin, B. Chimier, G. Duchateau, B. Chassagne, R. Kling, C. Hönninger, E. Mottay, and J. Lopez, Improved laser glass cutting by spatio-temporal control of energy deposition using bursts of femtosecond pulses, Opt. Express **25**, 33271 (2017).
[18] J. del Hoyo, R. Meyer, L. Furfaro, and F. Courvoisier, Nanoscale confinement of energy deposition in glass by double ultrafast Bessel pulses, Nanophotonics **10**, 1089 (2020).
[19] R. Beuton, B. Chimier, P. Quinoman, P. González Alaiza de Martínez, R. Nuter, and G. Duchateau, Numerical studies of dielectric material modifications by a femtosecond Bessel–Gauss laser beam, Appl. Phys. A **127**, 334 (2021).
[20] P. Gibbon and A. R. Bell, Collisionless absorption in sharp-edged plasmas, Phys. Rev. Lett. **68**, 1535 (1992).
[21] U. Teubner, J. Bergmann, B. van Wonterghem, F. P. Schäfer, and R. Sauerbrey, Angle-dependent X-ray emission and resonance absorption in a laser-produced plasma generated by a high intensity ultrashort pulse, Phys. Rev. Lett. **70**, 794 (1993).
[22] J. P. Palastro, J. G. Shaw, R. K. Follett, A. Colaïtis, D. Turnbull, A. V. Maximov, V. N. Goncharov, and D. H. Froula, Resonance absorption of a broadband laser pulse, Phys. Plasmas **25**, 123104 (2018).
[23] Y. Ping, R. Shepherd, B. F. Lasinski, M. Tabak, H. Chen, H. K. Chung, K. B. Fournier, S. B. Hansen, A. Kemp, D. A. Liedahl, K. Widmann, S. C. Wilks, W. Rozmus, and M. Sherlock, Absorption of short laser pulses on solid targets in the ultrarelativistic regime, Phys. Rev. Lett. **100**, 085004 (2008).
[24] T. D. Arber, K. Bennett, C. S. Brady, A. Lawrence-Douglas, M. G. Ramsay, N. J. Sircombe, P. Gillies, R. G. Evans, H. Schmitz, A. R. Bell, and C. P. Ridgers, Contemporary particle-in-cell approach to laser-plasma modelling, Plasma Phys. Controlled Fusion **57**, 113001 (2015).
[25] K. Ardaneh, R. Giust, B. Morel, and F. Courvoisier, Generation of a Bessel beam in FDTD using a cylindrical antenna, Opt. Express **28**, 2895 (2020).
[26] V. R. Bhardwaj, E. Simova, P. P. Rajeev, C. Hnatovsky, R. S. Taylor, D. M. Rayner, and P. B. Corkum, Optically produced arrays of planar nanostructures inside fused silica, Phys. Rev. Lett. **96**, 057404 (2006).
[27] Y. Liao, J. Ni, L. Qiao, M. Huang, Y. Bellouard, K. Sugioka, and Y. Cheng, High-fidelity visualization of formation of volume nanogratings in porous glass by femtosecond laser irradiation, Optica **2**, 329 (2015).
[28] See Supplemental Material at http://link.aps.org/supplemental/10.1103/k23j-c9y7 for additional experimental and simulation results, detailed analysis of plasma scattering, and detailed analysis of lobe shift from near field fluence, which includes Refs. [18,24,29–35].
[29] S. Khadir, P. C. Chaumet, G. Baffou, and A. Sentenac, Quantitative model of the image of a radiating dipole through a microscope, J. Opt. Soc. Am. A **36**, 478 (2019).
[30] C. F. Bohren and D. R. Huffman, *Absorption and Scattering of Light by Small Particles* (John Wiley & Sons Ltd, New York, 1998).
[31] C. Xie, V. Jukna, C. Milián, R. Giust, I. Ouadghiri-Idrissi, T. Itina, J. M. Dudley, A. Couairon, and F. Courvoisier, Tubular filamentation for laser material processing, Sci. Rep. **5**, 8914 (2015).
[32] J. D. Jackson, *Classical Electrodynamics*, 3rd ed. (Wiley, Hoboken, NJ, 1998).
[33] P. Yeh, A. Yariv, and E. Marom, Theory of Bragg fiber, J. Opt. Soc. Am. **68**, 1196 (1978).
[34] P. Y. Yu and M. Cardona, *Fundamentals of Semiconductors: Physics and Materials Properties* (Springer, Berlin, Heidelberg, 2010).
[35] M. Chanal, V. Y. Fedorov, M. Chambonneau, R. Clady, S. Tzortzakis, and D. Grojo, Crossing the threshold of ultrafast laser writing in bulk silicon, Nat. Commun. **8**, 773 (2017).
[36] L. Sudrie, A. Couairon, M. Franco, B. Lamouroux, B. Prade, S. Tzortzakis, and A. Mysyrowicz, Femtosecond laser-induced damage and filamentary propagation in fused silica, Phys. Rev. Lett. **89**, 186601 (2002).
[37] K. Bergner, B. Seyfarth, K. A. Lammers, T. Ullsperger, S. Döring, M. Heinrich, M. Kumkar, D. Flamm, A. Tünnermann, and S. Nolte, Spatio-temporal analysis of glass volume processing using ultrashort laser pulses, Appl. Opt. **57**, 4618 (2018).

[38] W. Kruer, *The Physics of Laser Plasma Interactions*, Frontiers in physics (Westview Press, Boulder, Colorado, 1988).
[39] R. Boyd and D. Prato, *Nonlinear Optics* (Academic Press, Cambridge, Massachusetts, 2008).
[40] B. Morel, R. Giust, K. Ardaneh, and F. Courvoisier, Two-fluid plasma model for ultrashort laser-induced electron-hole nanoplasmas, Phys. Rev. B **106**, 035207 (2022).
[41] M. Kauranen and A. V. Zayats, Nonlinear plasmonics, Nat. Photonics **6**, 737 (2012).
[42] M. Z. Alam, I. De Leon, and R. W. Boyd, Large optical nonlinearity of indium tin oxide in its epsilon-near-zero region, Science **352**, 795 (2016).
[43] T. Kampfrath, K. Tanaka, and K. A. Nelson, Resonant and nonresonant control over matter and light by intense terahertz transients, Nat. Photonics **7**, 680 (2013).
[44] S. Han, H. Kim, Y. W. Kim, Y.-J. Kim, S. Kim, I.-Y. Park, and S.-W. Kim, High-harmonic generation by field enhanced femtosecond pulses in metal-sapphire nanostructure, Nat. Commun. **7**, 13105 (2016).
[45] A. Denoeud, A. Benuzzi-Mounaix, A. Ravasio, F. Dorchies, P. M. Leguay, J. Gaudin, F. Guyot, E. Brambrink, M. Koenig, S. Le Pape, and S. Mazevet, Metallization of warm dense SiO_2 studied by XANES spectroscopy, Phys. Rev. Lett. **113**, 116404 (2014).
[46] R. Ernstorfer, M. Harb, C. T. Hebeisen, G. Sciaini, T. Dartigalongue, and R. D. Miller, The formation of warm dense matter: Experimental evidence for electronic bond hardening in gold, Science **323**, 1033 (2009).
[47] https://cfsa-pmw.warwick.ac.uk.

End Matter

Experiments—Figure 4 shows our experimental setup. We spatially shaped laser pulses at a central wavelength of 800 nm. Using a spatial light modulator (SLM) combined to a 2f-2f telecentric arrangement, we produce a Bessel beam with cone angle 25° in air. The pulse duration of 100 fs has been characterized at the sample position. After the interaction with the 400 μm thick c-cut sapphire sample, the pulse is collected with a ×100 microscope objective (Olympus MPLFLN) in a 2f-2f arrangement to image the pulse on a 14 bits camera. The imaging system, with a numerical aperture of 0.9 is placed on an independent translation stage.

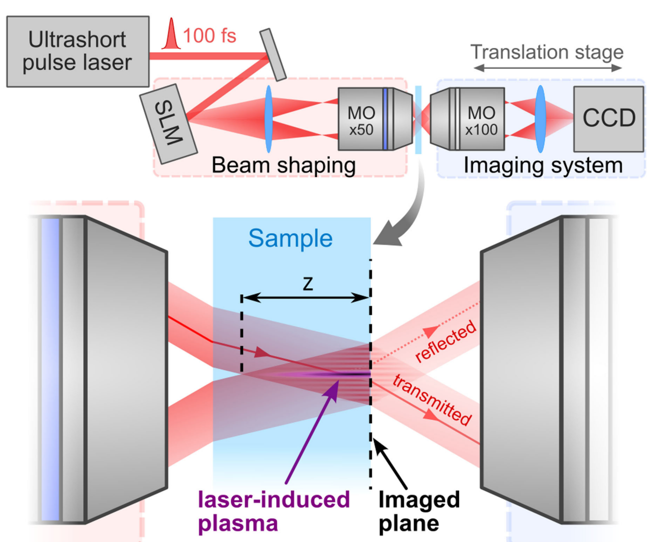

FIG. 4. Experimental setup. The Bessel beam propagates within the sample up to propagation distance z. It is then imaged onto the CCD camera by conjugating the exit side surface with the camera plane. In the bottom panel, a ray-tracing approach shows that reflected and transmitted fractions of the Bessel pulse on the plasma are collected by the imaging system. SLM: spatial light modulator; MO: microscope objective.

The relative position of the Bessel beam within the sample is adjusted, using the sample translation stage, to cross the exit surface. This effectively interrupts the nonlinear propagation at a controlled propagation distance z corresponding to the distance between the Bessel beam onset and the exit surface. We image the near-field fluence distribution of the exit surface plane onto the camera. The mismatch between the focal plane of the collection microscope objective and the exit surface is typically ≤ 1 μm. The single-shot near-field distribution, as shown in Fig. 2, can be compared to numerical simulations of the fluence. This approach has already been validated [31] and used by other groups in different conditions [35].

To produce a 3D scan, we simultaneously shift the sample and the imaging setup, thus maintaining constant—within typically 1 μm—the distance between the exit side and microscope objective. Between two shots, we translate the sample in its plane to irradiate a fresh area of the sample.

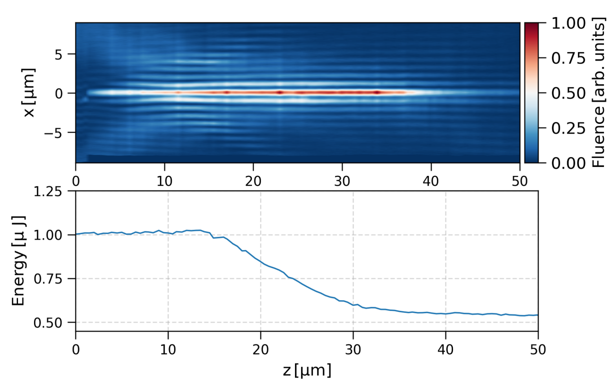

FIG. 5. Top: experimental distribution of the fluence with propagation, in xz plane, for a pulse energy of 1 μJ. Bottom: evolution of the pulse energy with propagation distance z, obtained by integration of the full pulse fluence recorded on the camera.

To obtain far-field images of Figs. 3(a) and 3(d), the last lens is replaced to conjugate the back focal plane of the imaging microscope with the camera.

Particle-in-cell simulations—

Pulse injection: Our numerical simulations model a plasma of electrons and ions (heavy holes) in vacuum. Our model corresponds to an electron-hole plasma with parabolic band approximation. The ions (holes) have a mass ratio of 102×1836, given by the product of the sapphire molar mass and the proton mass. In our simulations, we note that the ions movement is negligible over the simulation time. We injected from the $z = 0$ boundary a Gaussian pulse which propagates along the positive z–direction and is polarized along the x–direction. We applied a phase $\Phi(r) = -(2\pi/\lambda) r \sin\theta$ to the Gaussian beam, as is done experimentally using a spatial light modulator. The wavelength and cone angle are $\lambda = 0.8$ μm, 25°, respectively. The temporal profile of the beam is a Gaussian function with a width of 100 fs FWHM. The Gaussian beam waist is $w = 10$ μm. All simulations using a reduced cone angle, to simulate refraction, gave very similar results in terms of absorption and characteristics of near- and far-field patterns. The Bessel beam length has been reduced to ≈18 μm, by cropping the injected Gaussian beam, to reduce the simulation run time. The peak intensity in the Bessel zone is 6×10^{14} W/cm^2 in absence of plasma, i.e., on the same order of magnitude as in the experiments.

Plasma parameters: The axial (along the z-direction) plasma density profile of the plasma rod follows $\tanh(z/z_0)$ with $z_0 = 1$ μm. It shows a z-invariant density profile extending from approximately 2 μm away from the onset of the Bessel beam. The plasma in the xy plane follows a Gaussian profile. We have simulated the interaction with plasmas of circular and elliptical transverse sections. The plasma density distribution is given by $n(x, y) = n_{\max} \exp[-(x^2/w_x^2)] \exp[-(y^2/w_y^2)]$ where w_x and w_y are the characteristic widths along the x and y directions, respectively. The minimum density for the cells is $n_{\min} = 10^{-5} n_c$. The *critical radii* R_{cx} and R_{cy} are defined as the transverse distances where the density equals the critical plasma density n_c, i.e., where $n(x, y) = n_c$. In our simulations, we tested a range of parameters: R_{cy} between 70 and 500 nm, R_{cx} between 25 and 200 nm, and maximum plasma densities $n_{\max}$ between $5n_c$ and $10n_c$. These values were chosen to explore the sensitivity of the interaction to the transverse plasma profile and to ensure consistency with experimentally relevant conditions. The velocity distribution of both plasma species have been initialized with a Maxwellian distribution at $T_e = T_i$. We have run simulations for different initial plasma temperatures of 1×10^{-3}, 1 and 10 eV and we have obtained very similar results in terms of pulse absorption, structure of the fields, and hot electron population. All simulations results have included collisions, although the collisionless case is almost indistinguishable.

Resolution: We have used a computational box of volume $15 \times 15 \times 30$ μm^3 and run the simulations up to $t_{\text{run}} = 320$ fs. The spatial resolution of the grid for second-order FDTD (finite-difference time domain) is set so that $dx k_r^0 = dy k_r^0 = 0.04$, and $dz k_z^0 = 0.1$ ($N_x \times N_y \times N_z = 1136 \times 1136 \times 706$), where $k_r^0 = k_0 \sin\theta$, $k_z^0 = k_0 \cos\theta$. Using a fourth-order FDTD solver has not shown any significant change in the results. The temporal resolution is constrained by the Courant stability condition. We have used the convolutional perfectly matched layers boundary conditions for the fields and open boundary conditions for the particles. After testing the simulations with different numbers of particles per cell from 32 to 128 to ensure energy conservation, we have chosen 32 (i.e., 16 per specie) particles per cell for a total number of 550 million particles per specie. Note that not all cells of the computation box are active. The $\sim 33 \times 10^6$ active cells are located in the volume of the plasma rod and contain overall ~500 million particles for each specie. We have used a triangle shape function with three points per axis, i.e., 27 grid points to calculate the electric current induced by each particle on the grid. We have obtained similar results using a third-order B-spline particle shape with five points per axis (125 points for 3D grid). In the simulation of laser-plasma interaction using PIC simulation, the Debye length with typical value in the range 0.2–2 nm is not resolved by the grid cell, as it is the case in most simulations of laser-solid interaction [24]. However, the energy is conserved using the energy conservative scheme for the integration of particle trajectory. In the EPOCH PIC code, the numerical heating is reported to grow as $\mathrm{d}T_{\mathrm{eV}}/\mathrm{d}t_{\mathrm{ps}} = \alpha_H n_{23}^{3/2} \Delta x_{\mathrm{nm}}^2 / n_{\mathrm{ppc}}$ where T_{eV} is the temperature in eV, t_{ps} time in ps, n_{23} density in 10^{23} cm^{-3}, Δx_{nm} grid cell in nm, n_{ppc} number of particles per cell, and α_H depends on the particle shape and current smoothing. For the triangular particle shape with current smoothing and the above resolutions $\alpha_H = 60$. Therefore, for the chosen resolution $\mathrm{d}T_{\mathrm{eV}}/\mathrm{d}t \sim 1$ eV/ps.

Far-field distributions for first and second harmonics— We have obtained the intensity spectrum $I(\omega, k_x, k_y)$ by performing a discrete Fourier transform on $B_{x:y:z}(t, x, y)$ at a fixed propagation distance of $z = 20$ μm (end of the constructed Bessel beam). The Fourier transformation has been performed on the recorded data for $|x| \leq 5$ μm and $|y| \leqslant 5$ μm. This is the reason for the relatively thick width of the simulation far-fields in Figs. 3(c) and 3(d). The first and second harmonic radiation spectra are then obtained by filtering the power spectrum at the central frequency of the pulse ω_0, and $2\omega_0$, respectively.